TARGET DESCRIPTION USING THE FULL-POLARIMETRIC SCATTERING SPECTRUM

Subhadip Dey[1], Noelia Romero-Puig[2], Avik Bhattacharya[3] and *Armando Marino[4]*

[1]Department of Agricultural and Food Engineering, Indian Institute of Technology Kharagpur, India
[2]Microwaves and Radar Institute, German Aerospace Center, Wessling, Germany
[3]Microwave Remote Sensing Lab, Indian Institute of Technology Bombay, Mumbai, India
[4]Earth Observation, Biological and Environmental Sciences, University of Stirling, United Kingdom

ABSTRACT

Several orthonormal projections onto various bases have been proposed to analyze Polarimetric Synthetic Aperture Radar (PolSAR) data. For target scattering characterization, these individual projections frequently lead to several additional ambiguities. Therefore, substantial confusion is commonly found when using unsupervised classification approaches to classify targets. In this study, we do not impose an orthogonality requirement and project the scattering information onto several realizations of the normalized scattering configuration. Using the full-polarimetric AIRSAR data over San Francisco, USA, we compute the spectrum of the scattering-type parameter, θ_{FP}, and go on to use this spectrum to categorize various land-cover targets.

Index Terms— Polarimetry, RADAR, synthetic aperture radar (SAR), scattering type parameter, spectrum analysis

1. INTRODUCTION

In Radar polarimetry, any invariant target characterization parameter is critical due to its ability to identify a target in varying basis sets (and therefore orientation conditions). This target characterization technique can be of two types: a) using coherent scattering information and b) using incoherent scattering information. Huynen [1] characterized a target using six different target parameters in his well-known phenomenological concept of radar target characterization.

The lack of global invariance is one of the main issues with the Huynen phenomenological radar target characterization. Once the roll-invariance limitation was removed, Cloude first draw attention to the global variance nature of the Huynen theory. In order to address this issue, Cloude and Pottier proposed the eigendecomposition of the coherency matrix [2]. This method yields a scattering entropy (H), a scattering anisotropy (A), and a target characterization parameter α.

While α can distinguish between some canonical targets, it cannot differentiate between any target, as for instance between a dihedral and a helical target. For this reason, Corr and Rodrigues [3] projected the scattering matrix onto a sphere, and two left- and right-handed helices bases. This approach was able to remove the ambiguity between the two targets. Touzi [4] suggested a new scattering vector model by projecting the Kennaugh-Huynen scattering matrix condiagonalization into the Pauli basis to address the limitations of the scattering-type parameter α. This model represents a radar target that is polarisation basis invariant in terms of five distinct target parameters. A roll-invariant scattering-type parameter (α_{GD}) was introduced by Ratha et al. [5] utilizing the geodesic distance between pairs of 4×4 real Kennaugh matrices.

Later, Dey et al. [6,7] presented θ_{FP} as a new target characterization parameter in the linear H—V basis. Similar to α, this roll-invariant parameter offers good target characterization capabilities. However, it also fails to discriminate between a helix or dihedral scattering. By projecting the scattering information onto several scattering bases, the current literature eliminates ambiguity. These projections, however, produced a variety of other uncertainties. As a result, in contrast to projections onto various orthonormal bases, it is necessary to produce the most information possible from the entire spectrum of scattering phenomena. Dey et al. [8] analyze the complete spectrum of θ_{FP} by projecting the incoherent coherency matrix onto several scattering mechanism bases. In this study, we have categorized several landcover classes using the θ_{FP} spectrum.

2. METHODOLOGY

The complete target scattering information for full-polarimetric SAR data is contained in the 2×2 scattering matrix, $\mathbf{S}$. However, this matrix cannot describe an incoherent target. As a result, the average of the elements of a scattering vector (e.g. Pauli) can be used to deduce the second-order information in terms of the coherency matrix, $\mathbf{T}$. This is achieved by using the Pauli basis matrices (Ψ). The Pauli vector ($\vec{\boldsymbol{k}}$) obtained by transforming the scattering matrix ($\mathbf{S}$) can be expressed as,

$$\mathbf{S} = \left[\begin{array}{cc} S_{\text{HH}} & S_{\text{HV}} \\ S_{\text{VH}} & S_{\text{VV}} \end{array} \right] \;\Rightarrow\; \vec{\boldsymbol{k}} = V([\mathbf{S}]) = \frac{1}{2}\text{Tr}(\mathbf{S}\Psi) \quad (1)$$
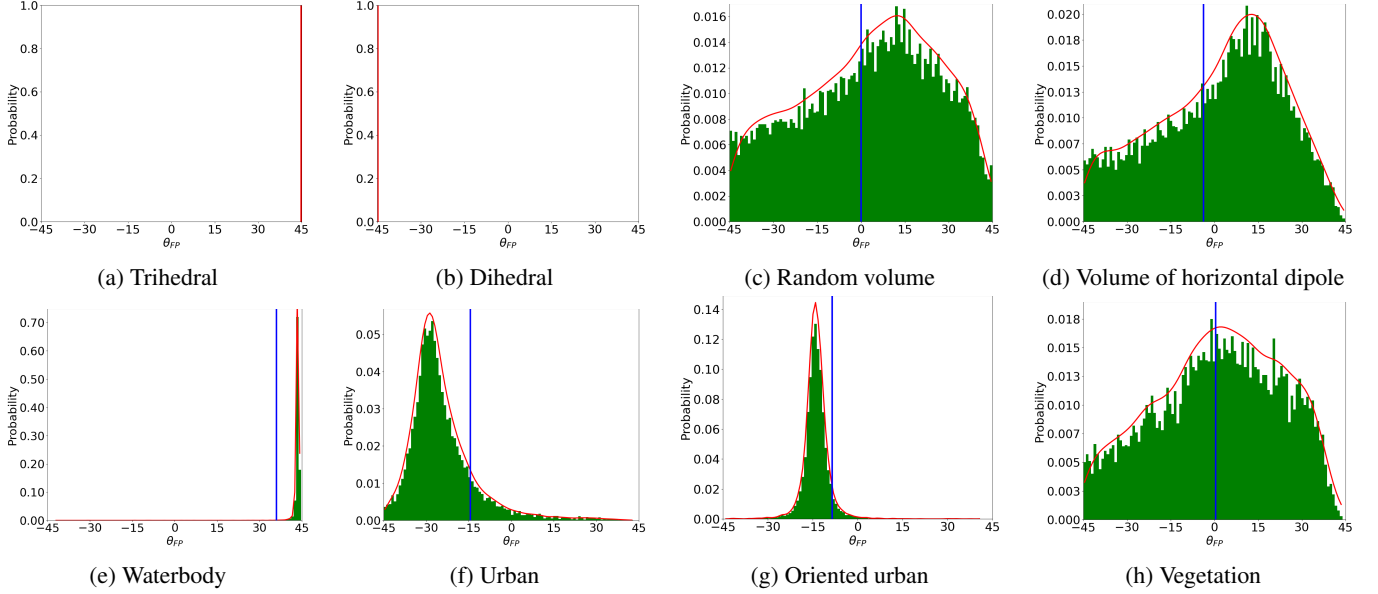
Fig. 1: Histogram of θ_{FP} (in degrees) for several canonical targets. The kernel-density estimate using the Gaussian kernels is represented by the red bounding curve. $\widehat{\alpha} = 45° - \overline{\alpha}$ is represented by the vertical blue line.

where $V(\cdot)$ is the vectorization operator on the scattering matrix, and Tr is the sum of the diagonal elements of the matrix. This Pauli basis vector, $\vec{k}$ can be used to derive the 3×3 coherency matrix $\mathbf{T}$ by the ensemble average $\langle \cdot \rangle$ of the outer product of the scattering vector $\vec{k}$ with its conjugate transpose $\vec{k}^{*T}$. Therefore, the coherency matrix can be written as, $\mathbf{T} = \langle \vec{k}\,\vec{k}^{*T} \rangle$. In general, the reciprocal theorem dictates that the rank of $\mathbf{T}$ remains 3.

Now, this coherency matrix, $\mathbf{T}$ can be projected to any scattering mechanism basis as,

$$\vec{\omega}_s = \mathbf{T}\vec{\omega}_n \qquad (2)$$

where, $\vec{\omega}_n$ is the normalized scattering vector ($\vec{\omega}_n = \vec{\omega}/|\vec{\omega}|$) of a parameterized scattering mechanism, $\vec{\omega}$,

$$\vec{\omega} = \begin{bmatrix} Ae^{i\phi_1} \\ Be^{i\phi_2} \\ Ce^{i\phi_3} \end{bmatrix} \qquad (3)$$

where, A, B and C are the magnitudes of each component and ϕ_1, ϕ_2 and ϕ_3 are their phases, respectively. Since $\mathbf{T}$ is positive semi-definite, $\langle \vec{\omega}_n^* \vec{\omega}_s \rangle \geq 0$. Therefore, the direction of $\vec{\omega}_s$ is same as the direction of $\vec{\omega}_n$. It can be noted that $\vec{\omega}_s = \vec{\omega}_n$ if $\mathbf{T}$ is rank one,

Following this, we obtained extra information, $\mathbf{T}_s$ by utilizing the projected vector, $\vec{\omega}_s$ as,

$$\mathbf{T}_s = \langle \vec{\omega}_s \vec{\omega}_s^{*T} \rangle \qquad (4)$$

where $\mathbf{T}_s$ is Hermitian and positive semi-definite. The rank of $\mathbf{T}_s$ is 1. This representation can be transformed into second-order information by Theorem 1.

Theorem 1. *Let $\mathbf{A}$ be a positive semi-definite matrix (real or complex). Then, there is precisely one positive semi-definite (and hence symmetric) matrix $\mathbf{B}$ such that $\mathbf{A} = \mathbf{B}^*\mathbf{B}$.*

This means that $\mathbf{T}_s$ can be written as $\mathbf{T}_s = \mathbf{T}_p^* \mathbf{T}_p$. The square root of the matrix is calculated using the Schur factorization technique. The matrix $\mathbf{T}_p$ is unique and is called the principal square root matrix. Additionally, because $\mathbf{T}$ is defined as the outer product of the scattering vector represented in the Pauli matrix basis, $\mathbf{T}_p$ can be intrinsically linked to a canonical target representation on the same basis.

Further, the scattering-type parameter, θ_{FP}^p from the elements of $\mathbf{T}_p$ is derived as proposed by Dey et al., [6],

$$\tan \theta_{\mathrm{FP}}^p = \frac{m_{\mathrm{FP}} \, \mathrm{Span} \, (T_{11} - T_{22} - T_{33})}{T_{11} \, (T_{22} + T_{33}) + m_{\mathrm{FP}}^2 \, \mathrm{Span}^2} \qquad (5)$$

where, m_{FP} is the 3D Barakat degree of polarization [9] and T_{11}, T_{22} and T_{33} are the diagonal elements of $\mathbf{T}_p$ with Span $= T_{11} + T_{22} + T_{33}$. θ_{FP}^p varies within the range: $[-45°, 45°]$. For a pure dihedral target, $\theta_{\mathrm{FP}}^p = -45°$, and for a pure trihedral target, $\theta_{\mathrm{FP}}^p = 45°$.

2.1. Analysis over different scatterers

We have shown the polarimetric spectrum over several scattering targets in this section. We conducted 1000 simulated random realizations of the normalized scattering configuration $\vec{\omega}_n$ to get the spectrum. The median value of θ_{FP}^p was then calculated as the average over 20 iterations. Additionally, we compared the average scattering-type parameter $\overline{\alpha}$ [2]. The expression used in this work is $\widehat{\alpha} = 45° - \overline{\alpha}$. As a result, $\widehat{\alpha}$ likewise varies from $-45°$ to $45°$, as θ_{FP}^p.

2

It can be observed that for both trihedral and dihedral scatterers in Fig. 1a and Fig. 1b, the median values of θ_{FP}^p are $45°$ and $-45°$, respectively. These figures also show no variations of the polarimetric spectrum as both trihedral and dihedral scatterers are coherent, and hence, $\vec{\omega}_s = \vec{\omega}_n$. On the contrary, the spectrum of both random volume and volume of horizontal dipole scatterers in Fig. 1c and Fig. 1d lies in the whole range of θ_{FP}^p. The median values of θ_{FP}^p for both targets are around $4°$, while the value of $\widehat{\alpha}$ is centered around $0°$.

The polarimetric spectrum over different natural targets, such as waterbody, urban, oriented urban, and vegetation, are shown in Fig. 1e, Fig. 1f, Fig. 1g and Fig. 1h, respectively. It can be seen from Fig. 1e that the median value of θ_{FP}^p is $43.49°$ $\pm\,0.04°$, while $\widehat{\alpha} \approx 35°$. As the waterbody acts as a trihedral-type scatterer, we observe odd-bounce scattering characteristics from the surface. Moreover, the scattered wave from the waterbody remains with a high degree of polarization. Hence, the standard deviation histogram θ_{FP}^p remains very low with a negligible kurtosis value.

On the contrary, an urban target in Fig. 1f show the median value of θ_{FP}^p as $-27.24° \pm 0.72°$ and $\widehat{\alpha} \approx -15°$. In particular, urban areas produce double-bounce scattering due to its close to dihedral characteristics. Also, the histogram of θ_{FP}^p is right-tailed, which essentially infers that some of the buildings within the averaging cell are oriented at some angles to the radar line of sight. Similarly, over the oriented urban area in Fig. 1g, we observe the median value of the spectrum as $-14.03° \pm 0.41°$, indicating high cross-pol scattering contribution due to their oblique geometry to the radar line of sight. Primarily, it can be noted that for both urban and oriented urban targets, the coefficient of variation of the spectrum increases as compared to the waterbody.

The vegetation target in Fig. 1h shows similar characteristics as the random volume and volume of the horizontal dipole. The median value of θ_{FP}^p is $2.4° \pm 0.32°$, and $\widehat{\alpha}$ is centered around $0°$.

3. RESULTS AND DISCUSSION

As illustrated in Fig. 2, we employed C-band Full Polarimetric (FP) AIRSAR data over San Francisco (SF), USA. Using randomly chosen pixels, the median values for the urban area (abbreviated "U"), waterbody (abbreviated "W"), and vegetation (abbreviated "V") are calculated. Google Earth is used to create the ground truth data, as seen in Fig. 2b. In this case, we employed the unsupervised classification algorithm K-means clustering to categorize various landcover classes. The clustering outcomes are compared to the $\left(\theta_{\text{FP}}^{(1)}, \theta_{\text{FP}}^{(2)}, \theta_{\text{FP}}^{(3)}\right)$, and θ_{FP} spectrum. The three scattering mechanisms obtained from the elements of the three rank-1 coherency matrices following eigendecomposition are $\left(\theta_{\text{FP}}^{(1)}, \theta_{\text{FP}}^{(2)}, \theta_{\text{FP}}^{(3)}\right)$.

The median value of θ_{FP}^p over the ocean area is observed approximately as $37° \pm 0.14°$. Alternatively, the median value

(a) Pauli RGB   (b) Labelled classes
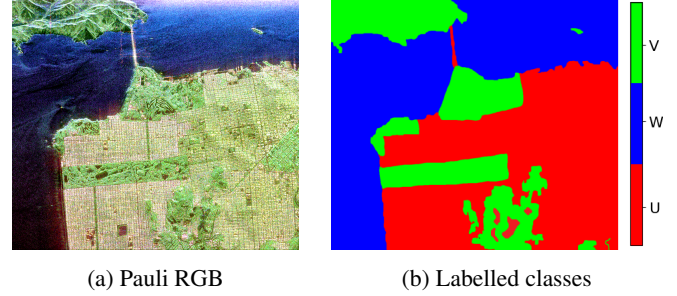
Fig. 2: AIRSAR data over the SF area. (a) Pauli RGB. (b) Labelled classes (U = Urban, W = Waterbody, and V = Vegetation).

of $\theta_{\text{FP}}^{(1)}$ is, approximately, $41°$, whereas the median values of $\theta_{\text{FP}}^{(2)}$ and $\theta_{\text{FP}}^{(3)}$ are around $-34°$. Over the urban area, the median value of θ_{FP}^p is $-24° \pm 4.2°$, depicting this area as an ensembles dihedral scatterer. We observe the median value of $\theta_{\text{FP}}^{(1)}$ around $-32° \pm 2.1°$ and the median value of $\theta_{\text{FP}}^{(2)}$ and $\theta_{\text{FP}}^{(3)}$ oscillate from $-11° \pm 4.2°$ to $37° \pm 6.4°$.

Over the vegetation area the median value of $\theta_{\text{FP}}^p \approx 6.2° \pm 3.2°$. The median value of $\theta_{\text{FP}}^{(1)}$ is around $9°$ to $16°$, approximately, and the mean values of $\theta_{\text{FP}}^{(2)}$ and $\theta_{\text{FP}}^{(3)}$ are approximately $20.4° \pm 6.2°$. Therefore, it can be seen that the values of $\theta_{\text{FP}}^{(1)}, \theta_{\text{FP}}^{(2)}$ and, $\theta_{\text{FP}}^{(3)}$ are similar over different landcover targets. At the same time, a prominent difference can be found in the histogram of θ_{FP}^p over the same landcover targets. Hence, the efficacy of θ_{FP}^p over $\theta_{\text{FP}}^{(1)}, \theta_{\text{FP}}^{(2)}$ and $\theta_{\text{FP}}^{(3)}$ is shown, quantitatively, in Table 1 and Table 2, respectively.

Table 1: Classification accuracy for the AIRSAR data over SF different for land cover targets using $\left(\theta_{\text{FP}}^{(1)}, \theta_{\text{FP}}^{(2)}, \theta_{\text{FP}}^{(3)}\right)$.

	Urban	Vegetation	Waterbody	Overall accuracy	Kappa score
UA	40.34%	11.46%	91.04%	51.10%	0.32
PA	60.31%	5.71%	61.03%		

The overall accuracy score of $\theta_{\text{FP}}^{(1)}, \theta_{\text{FP}}^{(2)}$ and $\theta_{\text{FP}}^{(3)}$ in Table 1 is $51.10\,\%$, while the overall accuracy score for θ_{FP}^p in Table 2, is $79.34\,\%$. Therefore, a general increase of around $30\,\%$ in the overall accuracy is observed using the θ_{FP}^p spectrum. The

Table 2: Classification accuracy for the AIRSAR data over SF different for land cover targets using the θ_{FP}^p spectrum.

	Urban	Vegetation	Waterbody	Overall accuracy	Kappa score
UA	51.41%	76.13%	82.81%	79.34%	0.64
PA	63.61%	54.42%	94.21%		

low accuracy score using $\theta_{\text{FP}}^{(1)}, \theta_{\text{FP}}^{(2)}$ and $\theta_{\text{FP}}^{(3)}$ than θ_{FP}^p spectrum might also be inferred using the t-distributed Stochastic Neighbor Embedding (t-SNE) plot in Fig. 3a and Fig. 3b. A high confusion occurs between waterbody and vegetation and

also between urban and vegetation for $\theta_{\text{FP}}^{(1)}$, $\theta_{\text{FP}}^{(2)}$ and $\theta_{\text{FP}}^{(3)}$ due to which low User's Accuracy (UA) and Producer's Accuracy (PA) is observed in Table 1. It can be observed that distinct clusters exist for waterbody, vegetation, and urban areas using the θ_{FP}^{p} spectrum. In contrast, such clusters are not as prominent in the case of $\left(\theta_{\text{FP}}^{(1)}, \theta_{\text{FP}}^{(2)}, \theta_{\text{FP}}^{(3)}\right)$.

(a) θ_{FP}^{p} spectrum (b) $\left(\theta_{\text{FP}}^{(1)}, \theta_{\text{FP}}^{(2)}, \theta_{\text{FP}}^{(3)}\right)$
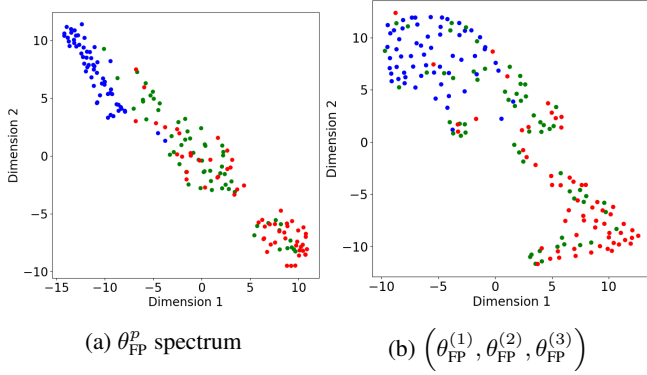
Fig. 3: t-SNE plot for the AIRSAR data over SF: (a) θ_{FP}^{p} spectrum and (b) $\left(\theta_{\text{FP}}^{(1)}, \theta_{\text{FP}}^{(2)}, \theta_{\text{FP}}^{(3)}\right)$. Red: urban, Green: Vegetation, and Blue: waterbody.

(a) $\left(\theta_{\text{FP}}^{(1)}, \theta_{\text{FP}}^{(2)}, \theta_{\text{FP}}^{(3)}\right)$ (b) θ_{FP}^{p} spectrum
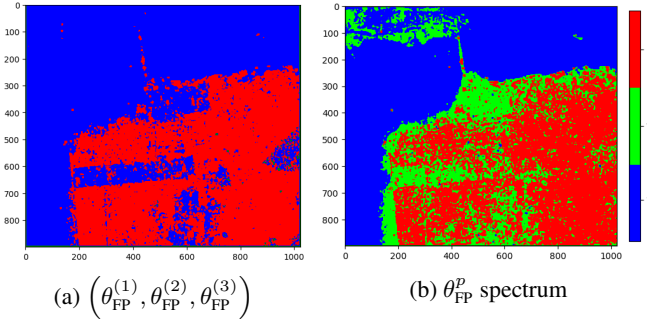
Fig. 4: Classification maps using RF for the AIRSAR SAR data over SF: (a) $\left(\theta_{\text{FP}}^{(1)}, \theta_{\text{FP}}^{(2)}, \theta_{\text{FP}}^{(3)}\right)$, and (b) θ_{FP}^{p} spectrum.

The classified maps of different landcover targets using AIRSAR C-band data are shown in Fig. 4. A high confusion was observed among urban, waterbody, and vegetation using $\left(\theta_{\text{FP}}^{(1)}, \theta_{\text{FP}}^{(2)}, \theta_{\text{FP}}^{(3)}\right)$. The classified map consists of a few number of vegetation pixels. In contrast, the classified map using θ_{FP}^{p} spectrum shows efficacy in distinguishing three landcover targets as compared to using $\left(\theta_{\text{FP}}^{(1)}, \theta_{\text{FP}}^{(2)}, \theta_{\text{FP}}^{(3)}\right)$.

4. CONCLUSIONS

In this study, the coherency matrix is projected onto various bases for non-orthogonal scattering mechanisms, and for each projection, the scattering-type parameter, θ_{FP}, is calculated, which is sensitive to the state of polarisation. With this

method, many scattering targets can be distinguished from one another while only requiring one physical parameter, θ_{FP}, as opposed to multiple statistical and physical parameters, such as $\overline{\alpha}$ and entropy. We compared this method to scattering processes at various eigen-polarization states, $\left(\theta_{\text{FP}}^{(1)}, \theta_{\text{FP}}^{(2)}, \theta_{\text{FP}}^{(3)}\right)$. The unsupervised classification is carried out using AIRSAR full-polarimetric SAR data over San Francisco, USA. According to the classification findings, the θ_{FP} spectrum outperforms the eigen-polarization states. The retrieval of soil moisture and monitoring of agricultural crops are two other uses for this unique approach.

5. REFERENCES

[1] J. R. Huynen, *Phenomenological theory of radar targets*, PhD dissertation, Technical Univ., Delf, The Netherlands, 1970.

[2] S. Cloude, *Polarisation: applications in remote sensing*, OUP Oxford, 2009.

[3] D. G. Corr and A. F. Rodrigues, "Alternative basis matrices for polarimetric decomposition," in *Proc. Eusar*, 2002, pp. 597–600.

[4] R. Touzi, "Target scattering decomposition in terms of roll-invariant target parameters," *IEEE Trans. Geosci. Remote Sens.*, vol. 45, no. 1, pp. 73–84, 2006.

[5] D. Ratha, E. Pottier, A. Bhattacharya, and A. C. Frery, "A polsar scattering power factorization framework and novel roll-invariant parameter-based unsupervised classification scheme using a geodesic distance," *IEEE Trans. Geosci. Remote Sens.*, pp. 1–17, 2019.

[6] S. Dey, A. Bhattacharya, D. Ratha, D. Mandal, and A. C. Frery, "Target characterization and scattering power decomposition for full and compact polarimetric SAR data," *IEEE Trans. Geosci. Remote Sens.*, vol. 59, no. 5, pp. 3981–3998, 2020.

[7] S. Dey, A. Bhattacharya, A. C. Frery, C. López-Martínez, and Y. S. Rao, "A model-free four component scattering power decomposition for polarimetric SAR data," *IEEE J. Sel. Top. Appl. Earth. Obs. Remote Sens.*, vol. 14, pp. 3887–3902, 2021.

[8] S. Dey, N. Romero-Puig, and A. Bhattacharya, "Polarimetric scattering spectrum analysis for target characterization," *IEEE Geosci. Remote Sens. Lett.*, vol. 19, pp. 1–5, 2022.

[9] R. Barakat, "n-fold polarization measures and associated thermodynamic entropy of N partially coherent pencils of radiation," *Opt. Acta*, vol. 30, no. 8, pp. 1171–1182, 1983.